

3DGSR: Implicit Surface Reconstruction with 3D Gaussian Splatting

XIAOYANG LYU and YANG-TIAN SUN, The University of Hong Kong, Hong Kong
 YI-HUA HUANG and XIUZHE WU, The University of Hong Kong, Hong Kong
 ZIYI YANG, Zhejiang University, China
 YILUN CHEN and JIANGMIAO PANG, Shanghai AI Lab, China
 XIAOJUAN QI, The University of Hong Kong, Hong Kong

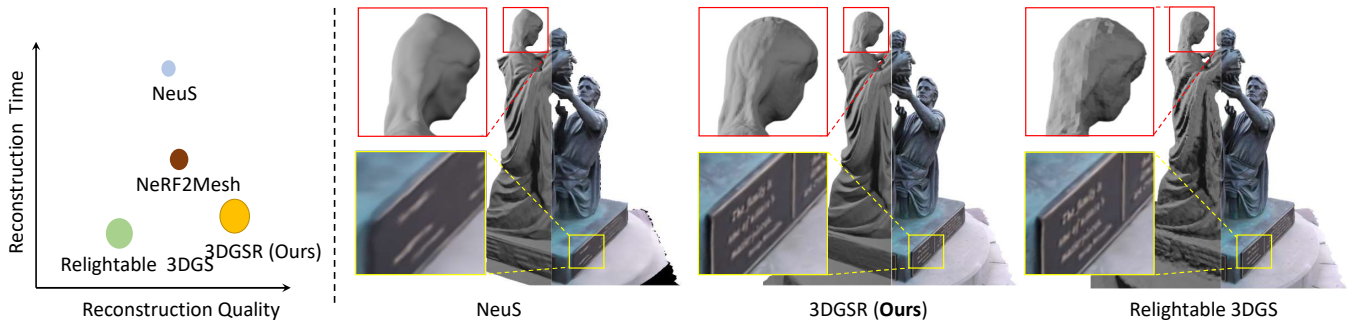


Fig. 1. Our method, called 3DGSR, achieves accurate 3D surface reconstruction with rich details, while maintaining the efficiency and high-quality rendering of 3DGS. The left part illustrates the performance comparison of 3DGSR with cutting-edge reconstruction methods. The right part shows the capability of our method to achieve high-quality reconstruction and rendering results simultaneously.

In this paper, we present an implicit surface reconstruction method with 3D Gaussian Splatting (3DGS), namely 3DGSR, that allows for accurate 3D reconstruction with intricate details while inheriting the high efficiency and rendering quality of 3DGS. The key insight is incorporating an implicit signed distance field (SDF) within 3D Gaussians to enable them to be aligned and jointly optimized. First, we introduce a differentiable SDF-to-opacity transformation function that converts SDF values into corresponding Gaussians' opacities. This function connects the SDF and 3D Gaussians, allowing for unified optimization and enforcing surface constraints on the 3D Gaussians. During learning, optimizing the 3D Gaussians provides supervisory signals for SDF learning, enabling the reconstruction of intricate details. However, this only provides sparse supervisory signals to the SDF at locations occupied by Gaussians, which is insufficient for learning a continuous SDF. Then, to address this limitation, we incorporate volumetric rendering and align the rendered geometric attributes (depth, normal) with those derived from 3D Gaussians. This consistency regularization introduces supervisory signals to locations not covered by discrete 3D Gaussians, effectively eliminating redundant surfaces outside the Gaussian sampling range. Our extensive experimental results demonstrate that our 3DGSR method enables high-quality 3D surface reconstruction while preserving the efficiency and

Authors' addresses: Xiaoyang Lyu; Yang-Tian Sun, The University of Hong Kong, Hong Kong; Yi-Hua Huang; Xiuzhe Wu, The University of Hong Kong, Hong Kong; Ziyi Yang, Zhejiang University, Hangzhou, China; Yilun Chen; Jiangmiao Pang, Shanghai AI Lab, Shanghai, China; Xiaojuan Qi, The University of Hong Kong, Hong Kong.

Permission to make digital or hard copies of all or part of this work for personal or classroom use is granted without fee provided that copies are not made or distributed for profit or commercial advantage and that copies bear this notice and the full citation on the first page. Copyrights for components of this work owned by others than ACM must be honored. Abstracting with credit is permitted. To copy otherwise, or republish, to post on servers or to redistribute to lists, requires prior specific permission and/or a fee. Request permissions from permissions@acm.org.

© 2024 Association for Computing Machinery.
 XXXX-XXXX/2024/4-ART \$15.00
<https://doi.org/10.1145/nnnnnnn.nnnnnnn>

rendering quality of 3DGS. Besides, our method competes favorably with leading surface reconstruction techniques while offering a more efficient learning process and much better rendering qualities. The code will be available at <https://github.com/CVMI-Lab/3DGSR>.

Additional Key Words and Phrases: Gaussian Splatting, Implicit Function, Signed Distance Function, Volumetric Rendering

ACM Reference Format:

Xiaoyang Lyu, Yang-Tian Sun, Yi-Hua Huang, Xiuzhe Wu, Ziyi Yang, Yilun Chen, Jiangmiao Pang, and Xiaojuan Qi. 2024. 3DGSR: Implicit Surface Reconstruction with 3D Gaussian Splatting. 1, 1 (April 2024), 10 pages. <https://doi.org/10.1145/nnnnnnn.nnnnnnn>

1 INTRODUCTION

3D Gaussian Splatting (3DGS) [Kerbl et al. 2023] has emerged as a new state-of-the-art approach for high-quality novel view synthesis. This method represents the geometry and appearance of a 3D scene as a set of Gaussians, which are then optimized from posed multi-view images. Thanks to its Gaussian rasterization pipeline, 3DGS achieves real-time efficiency, even when rendering high-resolution outputs. Despite its impressive rendering quality and efficiency, 3DGS generates only noisy, incomplete points for 3D geometry and struggles to accurately reconstruct the 3D surface of a scene [Tang et al. 2023a]. These, however, are highly desired in various geometry-related applications, such as 3D reconstruction, geometry editing, animation, and relighting, among others.

This motivates us to investigate how to enable 3DGS for high-quality surface reconstruction while preserving its rendering capabilities and speed. The inability of 3DGS to faithfully represent a 3D surface stems from its unstructured point-based geometry representation (i.e., the center of Gaussian). During optimization,

the positions of these points (Gaussians) are adjusted to capture the geometry of the scene. However, the learning objective is to improve the rendering quality, which may not necessarily lead to accurate positions. The limited number of views utilized for learning further exacerbates this issue. Besides, the optimization process does not consider the geometric constraints among the points that are indeed constrained by the underlying geometry (i.e., surfaces), leading to noisy points. Further, the discrete and unstructured points make it difficult to extract 3D surfaces through post-processing, such as Poisson surface reconstruction [Kazhdan and Hoppe 2013].

In this paper, we introduce 3DGSR, a novel approach that incorporates a neural implicit signed distance field (SDF) within Gaussians for geometry modeling, which is then jointly optimized and aligned with 3D Gaussians. First, we propose a differentiable SDF-to-opacity transformation function that converts SDF values into corresponding Gaussians' opacities, thus connecting SDF and Gaussians. This association enforces surface constraints on Gaussians, aligns the SDF with Gaussians, and facilitates their unified optimization. Next, during learning, optimizing the Gaussians will provide supervisory signals for updating the SDF, allowing the reconstruction of intricate details. However, this only offers sparse supervisory signals to the SDF at locations occupied by the Gaussians, which proves inadequate for optimizing a continuous SDF and may lead to the formation of redundant structures. To address this issue, we further integrate volumetric rendering [Mildenhall et al. 2021; Wang et al. 2021] and align the rendered depth (normal) with that obtained from 3D Gaussians through consistency loss to optimize the SDF. This approach effectively regularizes locations not covered by 3D Gaussians, eliminating unnecessary surface reconstructions beyond the Gaussian sampling range (see Fig. 3). It is worth noting that since we only sample a few rays during each learning iteration, this does not introduce significant computational costs. The coupled representation and learning of the 3D Gaussians and the implicit SDF field form a positive feedback cycle, enabling them to improve each other through mutual learning and ultimately yield high-quality rendering and surface reconstruction. As illustrated in Fig. 1, our approach achieves accurate reconstruction and high-quality rendering results simultaneously.

Comprehensive experiments conducted on various datasets show that our method is capable of producing high-quality reconstruction results while simultaneously preserving the efficiency and qualities of 3DGS. When compared to state-of-the-art methods for surface reconstruction [Tang et al. 2023b; Wang et al. 2021; Yariv et al. 2021], our approach substantially surpasses them in rendering quality and facilitates the reconstruction of intricate structures with significantly shorter learning time.

2 RELATED WORKS

Our method builds upon prior works in 3D reconstruction with multi-view images to enable fast surface reconstruction and novel view synthesis. We discuss prior works in multi-view 3D reconstruction, neural implicit representation, and point-based rendering.

Multi-view Stereo. Traditional multi-view stereo (MVS) methods have employed point-based [Barnes et al. 2009; Galliani et al. 2016;

Schönberger et al. 2016; Stereopsis 2010] and voxel-based [Broadhurst et al. 2001; De Bonet and Viola 1999; Seitz and Dyer 1999] representation. Point-based methods estimate the 3D positions of pixels by matching multi-view images and finding pixel correspondences. The surface can then be obtained by performing screened Poisson surface reconstruction [Kazhdan and Hoppe 2013] on the resulting point clouds. However, these methods heavily rely on matching accuracy and struggle to reconstruct textureless regions. On the other hand, voxel-based methods cannot achieve high-quality reconstruction due to the resolution limitation caused by high memory consumption.

Neural Implicit Representations. In recent years, the fields implicitly predicted by neural networks have gained significant attention in both novel view synthesis [Lombardi et al. 2019; Mildenhall et al. 2021; Sitzmann et al. 2019] and 3D reconstruction [Jiang et al. 2020; Kellnhofer et al. 2021; Liu et al. 2020b; Niemeyer et al. 2020; Yariv et al. 2020]. Neural Radiance Field (NeRF) [Mildenhall et al. 2021] has demonstrated excellent performance in high-quality novel view synthesis by modeling scenes with a density field and a view-dependent color field. However, NeRF's density field cannot extract high-quality surfaces. To achieve accurate surface reconstruction, NeuS [Wang et al. 2021] represents the scene with a signed distance function (SDF) and derives the alpha value from the precondition that the zero-level surface contributes the most to the volume rendering. Following NeuS, Darmon et al. [Darmon et al. 2022] improves the reconstruction quality with an additional warping loss that ensures photometric consistency. Neuralangelo [Li et al. 2023b] introduces multi-resolution hash grids [Müller et al. 2022] and regularizes the model with numerical gradients and coarse-to-fine training. However, these methods often require extensive training time, which can limit their practical applicability.

Several works have focused on accelerating neural implicit representation by using implicit-explicit hybrid representation with grids [Fridovich-Keil et al. 2022; Karnewar et al. 2022; Müller et al. 2022; Sun et al. 2022; Wang et al. 2023a], trees [Liu et al. 2020a; Yu et al. 2021], points [Chen et al. 2023b; Dai et al. 2023; Xu et al. 2022], or low-rank decomposition [Chan et al. 2022; Chen et al. 2022; Hu et al. 2023]. These methods speed up the training process and promote the rendering speed of radiance fields to a remarkable real-time level. However, fast and high-quality surface reconstruction from multi-view images remains a challenging problem.

Point-based Rendering. Unstructured points [Gross and Pfister 2011] can be efficiently rendered to obtain novel-view images. However, directly rasterizing colored point clouds [Grossman and Dally 1998] with fixed point sizes can lead to disconnected artifacts such as discontinuity, holes, and aliasing. To address these issues, previous works [Botsch et al. 2005; Pfister et al. 2000; Ren et al. 2002; Zwicker et al. 2001] extend points to larger primitives (e.g., spheres, ellipsoids, and surfels) and splat them onto the image plane. Differentiable point-based methods [Aliev et al. 2020; Pittaluga et al. 2019; Rakhimov et al. 2022] tackle these artifacts by rendering a holed latent feature map and then decoding it as a full RGB image using neural networks. Alternatively, some approaches render points as primitives (e.g., surfels and Gaussians) with trainable parameters

and render them differentially [Kerbl et al. 2023; Yifan et al. 2019; Zhang et al. 2022].

Most recently, 3D Gaussian Splatting (3DGS) [Kerbl et al. 2023] has demonstrated remarkable performance in terms of high-level rendering quality and real-time rendering. Subsequent works have extended 3DGS to handle 3D/4D generation [Ren et al. 2023; Tang et al. 2023a; Yang et al. 2023a; Yi et al. 2023; Zielonka et al. 2023], dynamic scenes [Das et al. 2023; Huang et al. 2023; Li et al. 2023a; Luiten et al. 2023; Yang et al. 2023b, 2024], relighting [Gao et al. 2023], and animation [Jung et al. 2023; Ye et al. 2023]. Some concurrent works [Chen et al. 2023a; Guédon and Lepetit 2023] aim to reconstruct the 3D surface from multi-view images using 3DGS. NeuSG [Chen et al. 2023a] jointly trains a NeuS [Wang et al. 2021] and 3DGS. During training, the normals derived from NeuS regularize the rotation of Gaussians, while NeuS is also regularized to ensure that the SDF values at Gaussians’ positions are close to zero. SuGaR [Guédon and Lepetit 2023] enforces Gaussians to have limited overlap with others during the optimization of 3DGS. After that, an initial mesh can be extracted by performing Poisson reconstruction [Kazhdan and Hoppe 2013] on Gaussians, using the shortest axis as normals. The mesh is then bound with flat Gaussians distributed on its faces and optimized to obtain refined results.

3 PRELIMINARIES

3D Gaussian Splatting (3DGS). 3DGS [Kerbl et al. 2023] employs 3D Gaussian points, characterized by a central point μ and a covariance matrix Σ , to effectively render images from given viewpoints:

$$G(x) = \exp\left(-\frac{1}{2}(x - \mu)^T \Sigma^{-1}(x - \mu)\right). \quad (1)$$

To facilitate optimization, Σ is factorized into the product of a scaling matrix S , represented by scale factors s , and a rotation matrix R encoded by a quaternion $r \in \mathbb{R}^4$:

$$\Sigma = RSS^T R^T, \quad (2)$$

For rendering novel views, the 3D Gaussians are projected onto a 2D image plane according to elliptical weighted average (EWA) [Zwicker et al. 2001]:

$$\Sigma' = JW\Sigma W^T J^T, \quad (3)$$

where W is the viewing transformation matrix, and J is the Jacobian derived from projective transformations. The final color $C(u)$ at pixel u is rendered by combining N ordered Gaussian splats using point-based α -blending:

$$C(u) = \sum_{i \in N} T_i \alpha_i c_i, \quad T_i = \prod_{j=1}^{i-1} (1 - \alpha_j). \quad (4)$$

Here, c_i is determined by the spherical harmonic (SH) function and the viewing direction, while α_i is computed from the 2D covariance Σ' , modulated by the opacity σ of each Gaussian [Kerbl et al. 2023]. In addition to rendering color c_i , Eq. (4) is also employed to render normal and depth as detailed below.

Normal and Depth Estimation from Gaussian. Typically, each 3D Gaussian can be treated as a conventional point cloud by using the centers of 3D Gaussians. Then, we can leverage the estimated

depth (normal) and render them into a depth (normal) map using point-based alpha blending [Gao et al. 2023] as:

$$\{\mathcal{D}, \mathcal{N}\} = \sum_{i \in N} T_i \alpha_i \{d_i, \mathbf{n}_i\}. \quad (5)$$

Here d_i and \mathbf{n}_i are the depth and normal of i th point respectively.

4 METHOD

Given posed multiview images $\{\mathcal{I}_k\}$ and a point cloud obtained from the Structure from Motion algorithm [Schönberger and Frahm 2016], our goal is to enable 3DGS with the ability to reconstruct accurate surface while preserving its rendering quality and efficiency. To accomplish this, we propose an approach integrating neural implicit signed distance field (SDF) within 3D Gaussians as shown in Fig. 2. A hash grid and a single-layer MLP are employed to predict the SDF value at each queried location. Additionally, we introduce a differentiable SDF-to-opacity transformation function Φ to link and align SDF and 3D Gaussians. Subsequently, given a 3D Gaussian, its opacity value is determined by querying the corresponding SDF value and transforming it using the function Φ . This coupled design allows the optimization of 3D Gaussians to supply supervisory signals for updating the SDF, enabling the reconstruction of intricate details. Details are unfolded in (Sec. 4.1).

However, the above is insufficient for optimizing the continuous SDF, as it can only provide supervision at locations where Gaussians are present. This results in floating artifacts in free space due to inadequate supervision (see Fig.3). To tackle this issue, we utilize volumetric rendering to generate depth and normals by querying points along the cast ray from the neural implicit SDF. Subsequently, a depth (normal) consistency loss is employed to align the rendered depth (normal) with those derived from 3D Gaussians, effectively regularizing the locations not covered by Gaussians and limiting floaters. The details are elaborated in 4.2.

4.1 Connect 3D Gaussians with Implicit SDF

The vanilla 3DGS method optimizes millions of Gaussians to accurately fit the training views, enabling photorealistic synthesis of novel views. However, its main emphasis is on fitting the target views, which does not guarantee high-quality 3D geometries. Moreover, the 3D Gaussians should be constrained by the underlying geometry (i.e., surfaces) of the 3D scene, which is absent in current methods. Consequently, 3DGS faces limitations in accurately reconstructing 3D surfaces (see Fig. 5).

Here, we introduce neural implicit SDF, denoted as $f: \mathbb{R}^3 \rightarrow \mathbb{R}^1$, which maps each 3D position $x \in \mathbb{R}^3$ to its signed distance from the target surface. This is implemented using multi-resolution hash grids [Müller et al. 2022] in conjunction with a single-layer MLP. The surface S of a scene can then be derived by using the zero-level set of its SDF, defined by:

$$S = \{x \in \mathbb{R}^3 \mid f(x) = 0\}. \quad (6)$$

Next, to link the SDF with 3D Gaussians, we introduce a differentiable SDF-to-opacity transformation function. This function should adhere to the constraint that points closer to the surface contribute more to rendering a pixel and, therefore, have a higher opacity value.

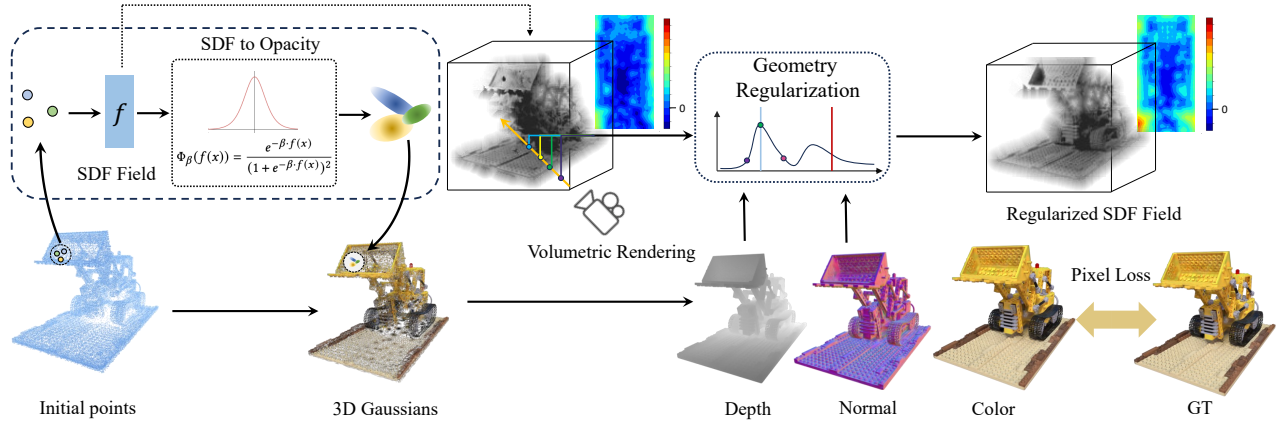


Fig. 2. Pipeline of our proposed approach for implicit surface reconstruction. We model the surface with an implicit SDF field, with which the SDF value of each 3D Gaussian can be predicted. The opacity of each Gaussian is modeled as a bell-shaped function of its distance to the implicit surface. The geometry attributes of 3D Gaussians serve as a regularization for the SDF field, while the rendered image is supervised by the captured image.

Consequently, we select a bell-shaped function $\Phi_\beta(f(x))$ controlled by a hyperparameter β , expressed as:

$$\Phi_\beta(f(x)) = \frac{e^{-\beta \cdot f(x)}}{(1 + e^{-\beta \cdot f(x)})^2}, \quad (7)$$

where β is a learnable parameter controlling the shape of the function.

This function transforms SDF values at a query location into the opacity of the corresponding Gaussian at that location. By linking the SDF with 3D Gaussians using a differentiable function, the SDF field can be updated through the optimization of 3D Gaussians by minimizing the photometric loss:

$$\mathcal{L}_c = \lambda \mathcal{L}_{D-SSIM} + (1 - \lambda) \mathcal{L}_1, \quad (8)$$

This loss function encourages the Gaussian at a location x that contributes more to rendering a pixel to have a higher opacity value $\Phi_\beta(f(x))$. This, in turn, encourages the SDF $f(x)$ to be closer to 0 and, therefore, nearer to the surface. The high-quality rendering capability of 3DGS allows for learning detailed image structures, which facilitates the reconstruction of detailed structures (see Fig. 5).

In addition to \mathcal{L}_c , we also impose a constraint as Eq. (9) to maintain consistency between the rendered normal \mathcal{N} , obtained directly from Gaussians via Eq. 5, and a pseudo normal $\hat{\mathcal{N}}$, computed from the rendered depth \mathcal{D} derived from 3D Gaussians under the local planarity assumption.

$$\mathcal{L}_n = \|\mathcal{N} - \hat{\mathcal{N}}\|_2. \quad (9)$$

Further, to encourage f to approximate a valid signed distance function, we follow the Eikonal equation [Gropp et al. 2020] to penalize the deviation of f :

$$\mathcal{L}_{\text{eik}} = \mathbb{E}_x [(\|\nabla f - 1\|)^2]. \quad (10)$$

Additionally, we enforce that the distribution of Gaussians adheres to the surface by constraining the SDF values at their centers to be close to zero:

$$\mathcal{L}_{\text{pt}} = \|f(x_g)\|_1, \quad (11)$$

where x_g denotes the centers of 3D Gaussians.

4.2 Regularization with Volumetric Rendering

By integrating the SDF field with 3D Gaussians and training them jointly, as discussed in Section 4.1, we can attain high-fidelity rendering results with an optimized SDF field. However, due to the sparse and discrete nature of 3D Gaussians, the aforementioned supervision signals are only available for locations occupied by 3D Gaussians, predominantly near the surface. This is insufficient to regularize the continuous SDF, resulting in artifacts at locations not covered by Gaussians, such as floating artifacts in unoccupied free spaces, as illustrated in Fig. 3.

Since volumetric rendering employs ray-casting to render a pixel, it samples points along a ray that includes both occupied and free points. We propose incorporating volumetric rendering for optimization. The depth map and normal map of volume rendering can effectively represent the occupancy distribution in the whole space, while those of sparse Gaussians aligns well with the observed image. This inspires us to adopt the rendering results of Gaussians' geometry attributes as the guidance of volume rendering, which can be utilized as the medium for propagating gradients. Specifically, we employ volumetric rendering to render depth (normals) and supervise them using depth (normals) derived from Gaussians using Eq. (5). This can provide regularizations to SDF values at locations uncovered by Gaussians.

More specifically, for each pixel, the ray cast from it is denoted as $\{\mathbf{p}(t) = \mathbf{r}_o + t \cdot \mathbf{r}_d \mid t > 0\}$, where \mathbf{r}_o is the camera center and \mathbf{r}_d is the unit direction vector of the ray. We accumulate the depth $\tilde{\mathcal{D}}(r)$ and normal $\tilde{\mathcal{N}}(r)$ along the cast ray [Wang et al. 2021]:

$$\tilde{\mathcal{D}}(r) = \sum_{i=1}^M T_i^r \alpha_i t_i^r, \quad \tilde{\mathcal{N}}(r) = \sum_{i=1}^M T_i^r \alpha_i \tilde{\mathbf{n}}_i^r, \quad (12)$$

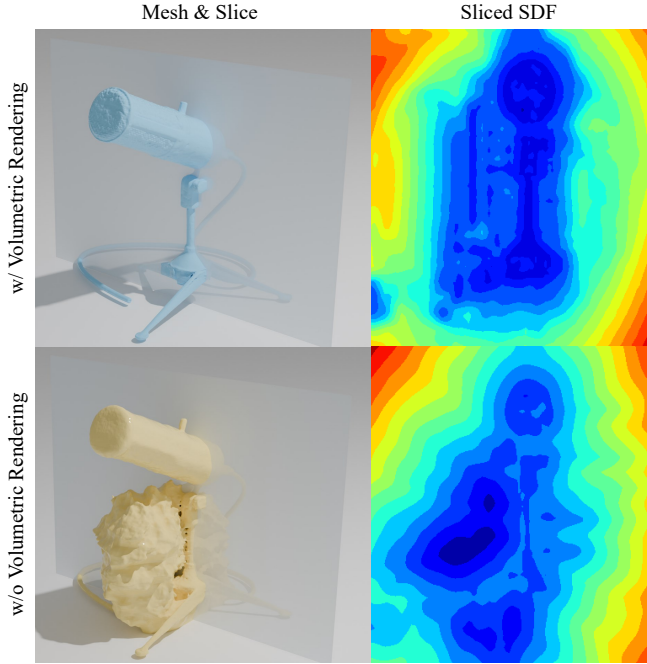


Fig. 3. Comparison of our method with and without volumetric rendering regularization. The incorporation of volumetric rendering regularization proves to be highly effective in eliminating floating artifacts in free space where Gaussians are absent.

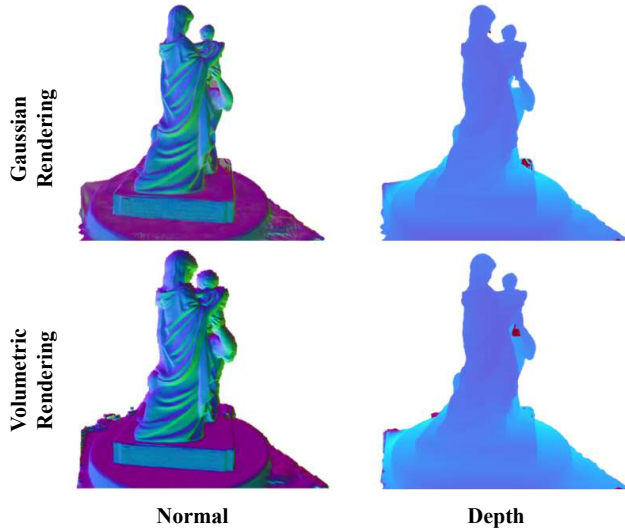


Fig. 4. Comparison of volume rendering results and Gaussian splatting results on the TNT dataset. The resemblance demonstrates the efficacy of our learning process in aligning the rendered geometric attributes - depth and normal - derived from volumetric rendering (which is based on the learned SDF) and those obtained from 3DGS.

where \tilde{n} is the normal computed by the gradient of SDF field ∇f , T_i^r and α_i represent the transmittance and alpha value (a.k.a opacity) of the sample point, and their values can be computed by

$$T_i^r = \prod_{j=1}^{i-1} (1 - \alpha_j), \quad \alpha_i = \max\left(\frac{\phi_s(f(x_i)) - \phi_s(f(x_{i+1}))}{\phi_s(f(x_i))}, 0\right), \quad (13)$$

where δ_i^r is the distance between adjacent sample points and ϕ_s is the Sigmoid function.

After that, we utilize the depth \mathcal{D} and normal \mathcal{N} rendered by Gaussian Splatting to supervise the volumetric rendering results \mathbf{D} and \mathbf{N} by optimizing the following objectives:

$$\mathcal{L}_{vd} = \sum_{r \in \mathcal{R}} \|\mathcal{D}(r) - \tilde{\mathbf{D}}(r)\|_2, \quad (14)$$

and

$$\mathcal{L}_{vn} = \sum_{r \in \mathcal{R}} \|\mathcal{N}(r) - \tilde{\mathbf{N}}(r)\|_1 + \|1 - \mathcal{N}(r)\tilde{\mathbf{N}}(r)\|_1, \quad (15)$$

where \mathcal{R} is the union of all training rays. These constraints regularize all the sampling points along the training rays, resulting in dense supervision for the implicit field and eliminating floating artifacts. As shown in Fig. 2, there exist noisy SDF distributions (negative value) floating over the free space between the camera and the object, which is then removed by applying the regularization with volumetric rendering. Accurate geometry can be obtained through our careful training strategy and model design. We visualize the optimized depth map and normal map of both volume rendering and Gaussian rendering in Fig 4.

The overall training objective is defined as a combination of all aforementioned losses:

$$\mathcal{L} = \mathcal{L}_c + \lambda_1 \mathcal{L}_n + \lambda_2 \mathcal{L}_{eik} + \lambda_3 \mathcal{L}_{pt} + \lambda_4 \mathcal{L}_{vd} + \lambda_5 \mathcal{L}_{vn}, \quad (16)$$

where $\lambda_1, \lambda_2, \lambda_3, \lambda_4, \lambda_5$ are hyperparameters that control the relative importance of each loss term.

5 EXPERIMENTS

5.1 Experimental Settings

Datasets. Our evaluation encompasses three datasets: the NeRF synthetic dataset [Mildenhall et al. 2021], the DTU real-captured dataset [Jensen et al. 2014], and the Tanks&Temples (TNT) large-scale dataset [Knapitsch et al. 2017]. The NeRF synthetic dataset consists of eight objects, each rendered via path tracing to generate 100 views. For testing, we select an eighth of these images, allocating the remainder for training. The DTU and TNT datasets are processed for camera poses as per [Gao et al. 2023], with image and mask processing following the methodology outlined in [Liu et al. 2020a]. The image resolutions for the DTU and TNT datasets are 1600×1200 and 1920×1080 pixels, respectively.

Comparisons. We evaluated our method from both surface reconstruction quality and rendering quality of novel-view synthesis. We benchmark our algorithm against several state-of-the-art methods, including NeRF [Mildenhall et al. 2021], NeuS [Wang et al. 2021], NeuSG [Chen et al. 2023a], RelighableGaussian [Gao et al. 2023], and NeRF2Mesh [Tang et al. 2023b], Neuralangelo [Li et al. 2023b], PET-NeuS [Wang et al. 2023b], BakedSDF [Yariv et al. 2023],

VolSDF [Yariv et al. 2021]. The quality of image synthesis is quantified using the Peak Signal-to-Noise Ratio (PSNR). For surface reconstruction accuracy, we employ the Chamfer distance and the F1 score as our metrics [Knapitsch et al. 2017]. Furthermore, we also compare the rendering quality of our method with some works that solely focus on novel view synthesis tasks (Tri-MipRF [Hu et al. 2023], Zip-NeRF [Barron et al. 2023], 3DGS [Kerbl et al. 2023]).

Implementation Details. Our work is implemented by PyTorch and CUDA and optimized by AdamW optimizer. We bind the Gaussian points to the SDF field for the whole training process to ensure that the Gaussian rendering process can provide a coarse SDF field, that can boost the converging speed of volumetric rendering. To ensure stable optimization, we introduce the warm-up strategy to make sure the dynamic Gaussian points can move around to the surface and provide an accurate supervised signal. The warm-up steps are set as 3000 for the Nerf synthetic dataset and 5000 for the TNT dataset. During the volumetric rendering stage, we sample $N = 1024$ rays per step.

For the synthetic data, we initialize the implicit function as a sphere, and the position of Gaussian is determined by the zero-level surface of the SDF field. For the real-world scenes, which frequently exhibit intricate geometry and noised pose, we adopt the SFM points as the initialized Gaussian position, and the network is still initialized as a sphere. Furthermore, we also apply the sparse MVS points to ensure the consistency between the rendered depth \mathcal{D} and projected depth map D_{mos} with \mathcal{L}_1 loss. Our models are trained for 30000 iterations, and all the experiments are conducted on a single NVIDIA GeForce RTX 3090 GPU.

5.2 Ablation Study

We conduct ablation studies on the NeRF Synthetic dataset in Table 3 to evaluate the effectiveness of each module in our method. Six different configurations are investigated to train our model.

Volumetric Constraints. The volumetric constraints have a minimal impact on novel view synthesis (PSNR: 32.83-33.32) yet significantly influence the reconstruction results (Chamfer-L1: 3.63-1.51). Both 3DGS rasterization and ray-based volumetric rendering rely on image supervision. However, the depth and normal representations derived from these dual methods exhibit distinct characteristics. While 3DGS excels at capturing high-frequency signals, it often suffers from floaters. Conversely, ray-based volumetric rendering yields smoother and more stable outcomes, but may struggle to capture fine details.

These two methods can complement each other and help address their respective weaknesses. Redundant Gaussian points can be effectively eliminated, and simultaneously, the high-frequency information learned by 3DGS can be employed to enhance the quality of the SDF field. This is demonstrated in Table 1 and Figure 3 of the main paper.

Learnable β . By making β trainable results, the conversion from SDF to 3DGS opacity can be learned automatically, which results in a 0.20 and 0.44 improvement in rendering and reconstruction performance, respectively.

Normal Supervision. If we use the pseudo normal to supervise the normal of Gaussian points, the model will get 0.23 and 0.05 improvement in Chamfer- \mathcal{L}_1 and PSNR, respectively.

Eikonal Loss. Removing the eikonal loss (Eq. (10)) will relax the constraint of SDF field, which can damage the surface learning and lead to worse reconstruction results. Note that better rendering quality (PSNR 33.4) is obtained in this configuration, which indicates the relaxation of geometric constraints in specific ways can aid in improving rendering quality.

Surface Alignment. Constraining the Gaussian points close to the zero-level surface will inject more high-frequency information into the SDF field leading to detailed surface extracted results.

Reconstruction Strategy. Compared with the marching cube with the SDF field, we also employ Poisson reconstruction to extract the surface from Gaussians with normals derived from the implicit SDF field, which exhibits a lower performance. This can be attributed to the noisy, sparse distribution of Gaussians that significantly impact the surface reconstruction quality. In contrast, the implicit SDF field provides a continuous representation, allowing for easy extraction of high-fidelity surfaces.

5.3 Experimental Results

Tables 1 and 2 present the quantitative results for synthetic and real-world datasets, respectively. On synthetic data, Table 1 demonstrates that our method surpasses other state-of-the-art methods in terms of the reconstruction quality, as measured by Chamfer- \mathcal{L}_1 distance. Furthermore, our method also excels in synthesizing high-quality novel view images, which are comparable to state-of-the-art novel view synthesis methods. This highlights our method’s superiority over surface reconstruction techniques and its competitive performance in novel view synthesis tasks. On real-captured DTU datasets, as shown in Table 2, our method also exhibits the best performance in terms of average surface reconstruction quality.

Besides, we also found that better reconstruction results have less contribution to the rendering quality compared to the vanilla 3DGS. The slightly lower performance is because 3DGS is optimized solely for rendering images; while our geometry constraints reduce the freedom of the optimization of 3DGS for the rendering tasks, the best solution for rendering may not necessarily be for geometry, as evidenced by performance in Table 1 (Trade-off between rendering quality and surface reconstruction). But overall, our formulation achieves the best trade-off between rendering quality and reconstruction quality.

Additionally, we provide qualitative comparisons of the reconstruction results qualitatively and present them in Figure 5. The state-of-the-art NeRF-based 3D reconstruction method NeRF2Mesh [Tang et al. 2023b] fails to preserve fine details like fine Mic textures, Lego tracks, and stripes on the Hotdog disk. RelightableGaussian [Gao et al. 2023] incorporates shading equations to determine Gaussian appearance and trains 3D Gaussians with attributes of normal and BRDF. 3D surfaces can then be obtained by applying Screened Poisson Reconstruction [Kazhdan and Hoppe 2013] on the 3D Gaussians assigned with normal. However, Gaussians are naturally discontinuous and unstructured, resulting in broken parts on the Mic and

		Chair	Drums	Ficus	Hotdog	Lego	Materials	Mic	Ship	Avg
PSNR	NeRF [Mildenhall et al. 2021]	34.17	25.08	30.39	36.82	33.31	30.03	34.78	29.30	31.74
	Ins-NGP [Müller et al. 2022]	35.00	26.02	33.51	37.40	36.39	29.78	36.22	31.10	33.18
	Mip-NeRF [Barron et al. 2021]	35.14	25.48	33.29	37.48	35.70	30.71	36.51	30.41	33.09
	3D-GS [Kerbl et al. 2023]	35.36	26.15	34.87	37.72	35.78	30.00	35.36	30.80	33.32
	NeuS [Wang et al. 2021]	31.22	24.85	27.38	36.04	34.06	29.59	31.56	26.94	30.20
	NeRO [Liu et al. 2023]	28.74	24.88	28.38	32.13	25.66	24.85	28.64	26.55	27.48
	BakedSDF [Yariv et al. 2023]	31.65	20.71	26.33	36.38	32.69	30.48	31.52	27.55	29.66
	NeRF2Mesh [Tang et al. 2023b]	34.25	25.04	30.08	35.70	34.90	26.26	32.63	29.47	30.88
	Ours	34.85	26.08	35.17	36.88	34.90	30.03	36.44	31.48	33.23
C- \mathcal{L}_1	VolSDF [Yariv et al. 2021]	1.18	4.03	3.01	3.22	2.26	1.57	1.13	6.42	2.86
	NeuS [Wang et al. 2021]	3.99	1.27	0.94	2.12	2.56	1.39	1.00	5.38	2.33
	NeRO [Liu et al. 2023]	1.27	1.97	1.22	1.88	1.90	1.33	0.87	4.95	1.92
	BakedSDF [Yariv et al. 2023]	1.83	1.43	1.09	1.68	1.13	1.36	0.84	3.88	1.66
	NeRF2Mesh [Tang et al. 2023b]	1.62	1.11	0.65	2.73	1.93	1.42	0.78	2.20	1.55
	RelightableGaussian [Gao et al. 2023]	3.65	2.34	1.26	3.11	1.63	1.35	1.76	3.35	2.31
	Ours	1.01	0.95	0.69	1.92	1.35	1.35	1.15	3.35	1.50

Table 1. We assess the quality of synthesized images and the accuracy of surface reconstruction, with each cell colored to indicate the **best** and **second best**. Our method is compared against various state-of-the-art (SOTA) approaches in tasks of novel view synthesis and surface reconstruction. It outperforms all competitors in both tasks, achieving the highest PSNR and the lowest Chamfer- \mathcal{L}_1 (C- \mathcal{L}_1) distance.

Scan ID	24	37	40	55	63	65	69	83	97	105	106	110	114	118	122	Mean
COLMAP	0.81	2.05	0.73	1.22	1.79	1.58	1.02	3.05	1.40	2.05	1.00	1.32	0.49	0.78	1.17	1.36
NeRF [Mildenhall et al. 2021]	1.90	1.60	1.85	0.58	2.28	1.27	1.47	1.67	2.05	1.07	0.88	2.53	1.06	1.15	0.96	1.49
NeuS [Wang et al. 2021]	1.00	1.37	0.93	0.43	1.10	0.65	0.57	1.48	1.09	0.83	0.52	1.20	0.35	0.49	0.54	0.84
VolSDF [Yariv et al. 2021]	1.14	1.26	0.81	0.49	1.25	0.70	0.72	1.29	1.18	0.70	0.66	1.08	0.42	0.61	0.55	0.86
ReGS [Gao et al. 2023]	1.21	1.00	1.10	0.87	1.03	1.51	1.51	1.06	1.63	0.97	1.36	1.21	0.94	1.38	1.26	1.20
Ours	0.68	0.84	0.70	0.39	1.16	0.87	0.77	1.48	1.26	0.87	0.69	0.80	0.42	0.64	0.60	0.81

Table 2. Quantitative assessment on the DTU dataset with each cell colored to indicate the **best** and **second best**. Our method achieves the highest average quality of surface reconstruction and the lowest Chamfer- \mathcal{L}_1 distance with real-world data.

Method	Chamfer- \mathcal{L}_1	F-score	PSNR	LPIPS	SSIM
w/o Geo	3.63	80.20	32.83	0.0380	0.963
static β	1.95	90.20	33.02	0.0385	0.966
w/o eq (9)	1.74	91.36	33.18	0.0383	0.967
w/o eq (10)	2.00	87.89	33.40	0.0350	0.968
w/o eq (11)	1.69	91.70	33.06	0.0388	0.966
Poisson	2.03	87.86	-	-	-
<i>Ours (full)</i>	1.51	93.50	33.23	0.0340	0.968

Table 3. Ablation study on the NeRF Synthetic dataset, where we evaluate the effect of each proposed component.

floaters on the Hotdog disk. Due to the absence of smooth surface modeling, its reconstructed results on Lego tracks, which contain intricate structures, are noisy and inaccurate. Combining the fitting power of Gaussian Splatting and the smooth surface modeling of the implicit SDF field, our method reconstructs surfaces with geometric details accurately and smoothly.

6 CONCLUSION

In this paper, we introduce 3DGSR, an efficient method for high-quality surface reconstruction using 3DGS. Our approach is based on two key components: 1) the integration of neural implicit SDF and its binding with 3D Gaussians through a differentiable SDF-to-opacity transformation function, and 2) the utilization of volumetric rendering and the SDF-and-Gaussian geometry consistency regularization for SDF optimization. The first component allows for the joint optimization of SDF and 3D Gaussians, with the optimization of Gaussians providing supervision signals for learning the SDF. The second component supplies additional supervision signals for refining the SDF in areas not occupied by Gaussians, using a consistency loss that aligns depth (normal) from SDF with that derived from Gaussians. Our extensive experiments showcase the effectiveness of 3DGSR in reconstructing high-quality surfaces outperforming those obtained from state-of-the-art reconstruction pipelines, without compromising the rendering capabilities and efficiency of 3D Gaussians. Our study does have certain limitations caused by the trade-off between rendering quality and surface smoothness. In

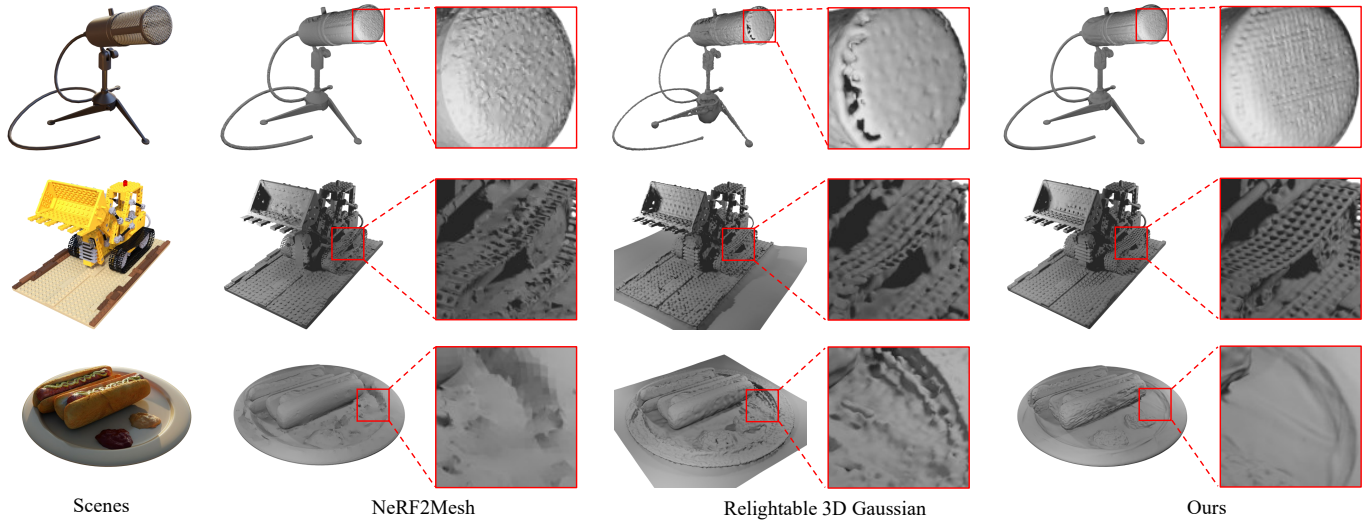


Fig. 5. Qualitative comparisons of reconstructed results between NeRF2Mesh [Tang et al. 2023b], Relightable 3D Gaussian [Gao et al. 2023], and our method on the NeRF Synthetic dataset. Our method yields the highest-quality surface reconstruction preserving fine details and intricate structures.

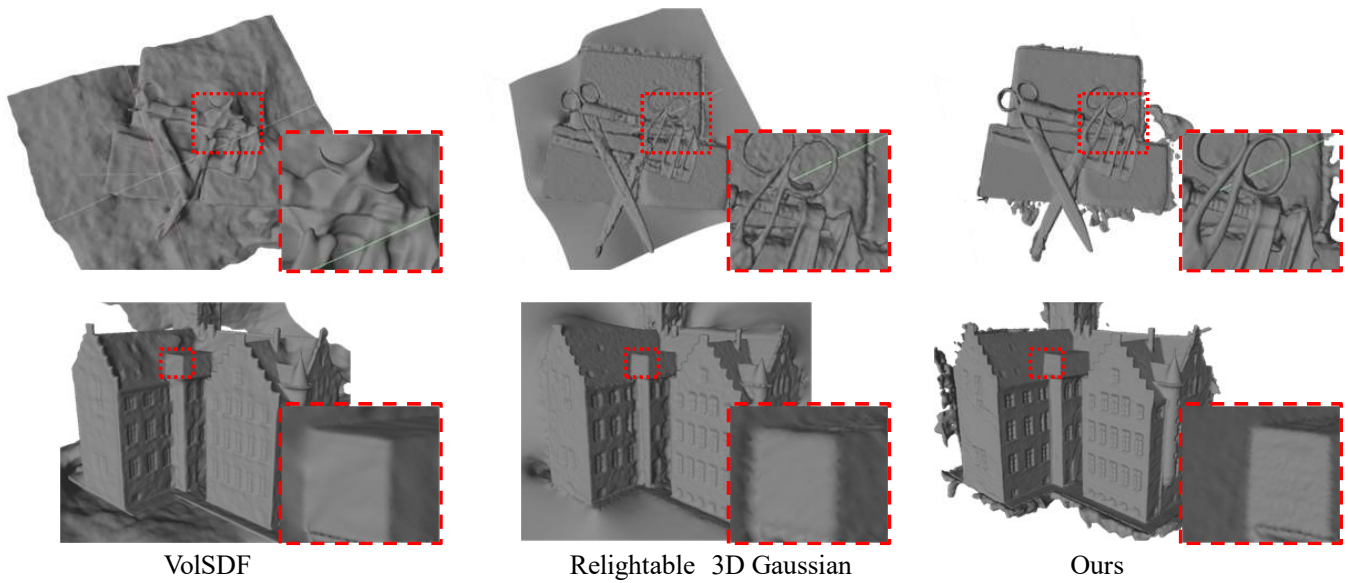


Fig. 6. Qualitative comparisons of reconstructed results between VoISDF [Yariv et al. 2021], Relightable 3D Gaussian [Gao et al. 2023], and our method on the DTU dataset. Our method yields the highest-quality surface reconstruction preserving fine details and intricate structures.

order to render high-quality images, the smoothness of the surface may be compromised in some cases involving complex texture patterns.

REFERENCES

Kara-Ali Aliev, Artem Sevastopolsky, Maria Kolos, Dmitry Ulyanov, and Victor Lempitsky. 2020. Neural point-based graphics. In *Computer Vision—ECCV 2020: 16th European Conference, Glasgow, UK, August 23–28, 2020, Proceedings, Part XXII 16*. Springer, 696–712.

Connelly Barnes, Eli Shechtman, Adam Finkelstein, and Dan B Goldman. 2009. Patch-Match: A randomized correspondence algorithm for structural image editing. *ACM*

Trans. Graph. 28, 3 (2009), 24.

Jonathan T Barron, Ben Mildenhall, Matthew Tancik, Peter Hedman, Ricardo Martin-Brualla, and Pratul P Srinivasan. 2021. Mip-nerf: A multiscale representation for anti-aliasing neural radiance fields. In *Proceedings of the IEEE/CVF International Conference on Computer Vision*. 5855–5864.

Jonathan T. Barron, Ben Mildenhall, Dor Verbin, Pratul P. Srinivasan, and Peter Hedman. 2023. Zip-NeRF: Anti-Aliased Grid-Based Neural Radiance Fields. *ICCV* (2023).

Mario Botsch, Alexander Hornung, Matthias Zwicker, and Leif Kobbelt. 2005. High-quality surface splatting on today’s GPUs. In *Proceedings Eurographics/IEEE VGTC Symposium Point-Based Graphics, 2005*. IEEE, 17–141.

Adrian Broadhurst, Tom W Drummond, and Roberto Cipolla. 2001. A probabilistic framework for space carving. In *Proceedings eighth IEEE international conference on*

- computer vision. *ICCV 2001*, Vol. 1. IEEE, 388–393.
- Eric R Chan, Connor Z Lin, Matthew A Chan, Koki Nagano, Boxiao Pan, Shalini De Mello, Orazio Gallo, Leonidas J Guibas, Jonathan Tremblay, Sameh Khamis, et al. 2022. Efficient geometry-aware 3D generative adversarial networks. In *Proceedings of the IEEE/CVF Conference on Computer Vision and Pattern Recognition*. 16123–16133.
- Anpei Chen, Zexiang Xu, Andreas Geiger, Jingyi Yu, and Hao Su. 2022. Tensorf: Tensorial radiance fields. In *European Conference on Computer Vision*. Springer, 333–350.
- Hanlin Chen, Chen Li, and Gim Hee Lee. 2023a. NeuSG: Neural Implicit Surface Reconstruction with 3D Gaussian Splatting Guidance. *arXiv preprint arXiv:2312.00846* (2023).
- Zhang Chen, Zhong Li, Liangchen Song, Lele Chen, Jingyi Yu, Junsong Yuan, and Yi Xu. 2023b. Neurf: A neural fields representation with adaptive radial basis functions. In *Proceedings of the IEEE/CVF International Conference on Computer Vision*. 4182–4194.
- Peng Dai, Yinda Zhang, Xin Yu, Xiaoyang Lyu, and Xiaojuan Qi. 2023. Hybrid Neural Rendering for Large-Scale Scenes with Motion Blur. In *Proceedings of the IEEE/CVF Conference on Computer Vision and Pattern Recognition*. 154–164.
- François Darmon, Bénédicte Bascle, Jean-Clément Devaux, Pascal Monasse, and Mathieu Aubry. 2022. Improving neural implicit surfaces geometry with patch warping. In *Proceedings of the IEEE/CVF Conference on Computer Vision and Pattern Recognition*. 6260–6269.
- Devikalyan Das, Christopher Wewer, Raza Yunus, Eddy Ilg, and Jan Eric Lenssen. 2023. Neural Parametric Gaussians for Monocular Non-Rigid Object Reconstruction. *arXiv preprint arXiv:2312.01196* (2023).
- Jeremy S De Bonet and Paul Viola. 1999. Poxels: Probabilistic voxelized volume reconstruction. In *Proceedings of International Conference on Computer Vision (ICCV)*, Vol. 2. 2.
- Sara Fridovich-Keil, Alex Yu, Matthew Tancik, Qinhong Chen, Benjamin Recht, and Angjoo Kanazawa. 2022. Plenoxels: Radiance fields without neural networks. In *Proceedings of the IEEE/CVF Conference on Computer Vision and Pattern Recognition*. 5501–5510.
- Silvano Galliani, Katrin Lasinger, and Konrad Schindler. 2016. Gipuma: Massively parallel multi-view stereo reconstruction. *Publikationen der Deutschen Gesellschaft für Photogrammetrie, Fernerkundung und Geoinformation e. V* 25, 361–369 (2016), 2.
- Jian Gao, Chun Gu, Youtian Lin, Hao Zhu, Xun Cao, Li Zhang, and Yao Yao. 2023. Relightable 3D Gaussian: Real-time Point Cloud Relighting with BRDF Decomposition and Ray Tracing. *arXiv preprint arXiv:2311.16043* (2023).
- Amos Gropp, Lior Yariv, Niv Haim, Matan Atzmon, and Yaron Lipman. 2020. Implicit Geometric Regularization for Learning Shapes. In *Proceedings of Machine Learning and Systems 2020*. 3569–3579.
- Markus Gross and Hanspeter Pfister. 2011. *Point-based graphics*. Elsevier.
- Jeffrey P Grossman and William J Dally. 1998. Point sample rendering. In *Rendering Techniques '98: Proceedings of the Eurographics Workshop in Vienna, Austria, June 29–July 1, 1998*. Springer, 181–192.
- Antoine Guédon and Vincent Lepetit. 2023. SuGaR: Surface-Aligned Gaussian Splatting for Efficient 3D Mesh Reconstruction and High-Quality Mesh Rendering. *arXiv preprint arXiv:2311.12775* (2023).
- Wenbo Hu, Yuling Wang, Lin Ma, Bangbang Yang, Lin Gao, Xiao Liu, and Yuewen Ma. 2023. Tri-miprf: Tri-mip representation for efficient anti-aliasing neural radiance fields. In *Proceedings of the IEEE/CVF International Conference on Computer Vision*. 19774–19783.
- Yi-Hua Huang, Yang-Tian Sun, Ziyi Yang, Xiaoyang Lyu, Yan-Pei Cao, and Xiaojuan Qi. 2023. SC-GS: Sparse-Controlled Gaussian Splatting for Editable Dynamic Scenes. *arXiv preprint arXiv:2312.14937* (2023).
- Rasmus Jensen, Anders Dahl, George Vogiatzis, Engin Tola, and Henrik Aanaes. 2014. Large scale multi-view stereopsis evaluation. In *Proceedings of the IEEE conference on computer vision and pattern recognition*. 406–413.
- Yue Jiang, Dantong Ji, Zhizhong Han, and Matthias Zwicker. 2020. Sdfdiff: Differentiable rendering of signed distance fields for 3d shape optimization. In *Proceedings of the IEEE/CVF conference on computer vision and pattern recognition*. 1251–1261.
- HyunJun Jung, Nikolas Brasch, Jifei Song, Eduardo Perez-Pellitero, Yiren Zhou, Zhihao Li, Nassir Navab, and Benjamin Busam. 2023. Deformable 3D Gaussian Splatting for Animatable Human Avatars. *arXiv preprint arXiv:2312.15059* (2023).
- Animesh Karnear, Tobias Ritschel, Oliver Wang, and Niloy Mitra. 2022. Relu fields: The little non-linearity that could. In *ACM SIGGRAPH 2022 Conference Proceedings*. 1–9.
- Michael Kazhdan and Hugues Hoppe. 2013. Screened poisson surface reconstruction. *ACM Transactions on Graphics (ToG)* 32, 3 (2013), 1–13.
- Petr Kellnhofer, Lars C Jebe, Andrew Jones, Ryan Spicer, Kari Pulli, and Gordon Wetzstein. 2021. Neural lumigraph rendering. In *Proceedings of the IEEE/CVF Conference on Computer Vision and Pattern Recognition*. 4287–4297.
- Bernhard Kerbl, Georgios Kopanas, Thomas Leimkühler, and George Drettakis. 2023. 3D Gaussian Splatting for Real-Time Radiance Field Rendering. *ACM Transactions on Graphics* 42, 4 (July 2023). <https://repo-sam.inria.fr/fungraph/3d-gaussian-splatting/>
- Arno Knapitsch, Jaesik Park, Qian-Yi Zhou, and Vladlen Koltun. 2017. Tanks and temples: Benchmarking large-scale scene reconstruction. *ACM Transactions on Graphics (ToG)* 36, 4 (2017), 1–13.
- Zhan Li, Zhang Chen, Zhong Li, and Yi Xu. 2023a. Spacetime Gaussian Feature Splatting for Real-Time Dynamic View Synthesis. *arXiv preprint arXiv:2312.16812* (2023).
- Zhaoshuo Li, Thomas Müller, Alex Evans, Russell H Taylor, Mathias Unberath, Ming-Yu Liu, and Chen-Hsuan Lin. 2023b. Neuralangelo: High-Fidelity Neural Surface Reconstruction. In *Proceedings of the IEEE/CVF Conference on Computer Vision and Pattern Recognition*. 8456–8465.
- Lingjie Liu, Jiatao Gu, Kyaw Zaw Lin, Tat-Seng Chua, and Christian Theobalt. 2020a. Neural sparse voxel fields. *Advances in Neural Information Processing Systems* 33 (2020), 15651–15663.
- Shaohui Liu, Yinda Zhang, Songyou Peng, Boxin Shi, Marc Pollefeys, and Zhaopeng Cui. 2020b. Dist: Rendering deep implicit signed distance function with differentiable sphere tracing. In *Proceedings of the IEEE/CVF Conference on Computer Vision and Pattern Recognition*. 2019–2028.
- Yuan Liu, Peng Wang, Cheng Lin, Xiaoxiao Long, Jiepeng Wang, Lingjie Liu, Taku Komura, and Wenping Wang. 2023. NeRo: Neural Geometry and BRDF Reconstruction of Reflective Objects from Multiview Images.
- Stephen Lombardi, Tomas Simon, Jason Saragih, Gabriel Schwartz, Andreas Lehrmann, and Yaser Sheikh. 2019. Neural volumes: learning dynamic renderable volumes from images. *ACM Transactions on Graphics (TOG)* 38, 4 (2019), 1–14.
- Jonathon Luiten, Georgios Kopanas, Bastian Leibe, and Deva Ramanan. 2023. Dynamic 3d gaussians: Tracking by persistent dynamic view synthesis. *arXiv preprint arXiv:2308.09713* (2023).
- Ben Mildenhall, Pratul P Srinivasan, Matthew Tancik, Jonathan T Barron, Ravi Ramamoorthi, and Ren Ng. 2021. Nerf: Representing scenes as neural radiance fields for view synthesis. *Commun. ACM* 65, 1 (2021), 99–106.
- Thomas Müller, Alex Evans, Christoph Schied, and Alexander Keller. 2022. Instant neural graphics primitives with a multiresolution hash encoding. *ACM Transactions on Graphics (ToG)* 41, 4 (2022), 1–15.
- Michael Niemeyer, Lars Mescheder, Michael Oechsle, and Andreas Geiger. 2020. Differentiable volumetric rendering: Learning implicit 3d representations without 3d supervision. In *Proceedings of the IEEE/CVF Conference on Computer Vision and Pattern Recognition*. 3504–3515.
- Hanspeter Pfister, Matthias Zwicker, Jeroen Van Baar, and Markus Gross. 2000. Surfels: Surface elements as rendering primitives. In *Proceedings of the 27th annual conference on Computer graphics and interactive techniques*. 335–342.
- Francesco Pittaluga, Sanjeev J Koppal, Sing Bing Kang, and Sudipta N Sinha. 2019. Revealing scenes by inverting structure from motion reconstructions. In *Proceedings of the IEEE/CVF Conference on Computer Vision and Pattern Recognition*. 145–154.
- Ruslan Rakhimov, Andrei-Timotei Ardelean, Victor Lempitsky, and Evgeny Burnaev. 2022. Npbg++: Accelerating neural point-based graphics. In *Proceedings of the IEEE/CVF Conference on Computer Vision and Pattern Recognition*. 15969–15979.
- Jiawei Ren, Liang Pan, Jiaxiang Tang, Chi Zhang, Ang Cao, Gang Zeng, and Ziwei Liu. 2023. DreamGaussian4D: Generative 4D Gaussian Splatting. *arXiv preprint arXiv:2312.17142* (2023).
- Liu Ren, Hanspeter Pfister, and Matthias Zwicker. 2002. Object space EWA surface splatting: A hardware accelerated approach to high quality point rendering. In *Computer Graphics Forum*, Vol. 21. Wiley Online Library, 461–470.
- Johannes Lutz Schönberger and Jan-Michael Frahm. 2016. Structure-from-Motion Revisited. In *Conference on Computer Vision and Pattern Recognition (CVPR)*.
- Johannes L Schönberger, Enliang Zheng, Jan-Michael Frahm, and Marc Pollefeys. 2016. Pixelwise view selection for unstructured multi-view stereo. In *Computer Vision—ECCV 2016: 14th European Conference, Amsterdam, The Netherlands, October 11–14, 2016, Proceedings, Part III* 14. Springer, 501–518.
- Steven M Seitz and Charles R Dyer. 1999. Photorealistic scene reconstruction by voxel coloring. *International Journal of Computer Vision* 35 (1999), 151–173.
- Vincent Sitzmann, Michael Zollhöfer, and Gordon Wetzstein. 2019. Scene representation networks: Continuous 3d-structure-aware neural scene representations. *Advances in Neural Information Processing Systems* 32 (2019).
- Robust Multiview Stereopsis. 2010. Accurate, Dense, and Robust Multiview Stereopsis. *IEEE TRANSACTIONS ON PATTERN ANALYSIS AND MACHINE INTELLIGENCE* 32, 8 (2010).
- Cheng Sun, Min Sun, and Hwann-Tzong Chen. 2022. Direct voxel grid optimization: Super-fast convergence for radiance fields reconstruction. In *Proceedings of the IEEE/CVF Conference on Computer Vision and Pattern Recognition*. 5459–5469.
- Jiaxiang Tang, Jiawei Ren, Hang Zhou, Ziwei Liu, and Gang Zeng. 2023a. DreamGaussian: Generative Gaussian Splatting for Efficient 3D Content Creation. *arXiv preprint arXiv:2309.16653* (2023).
- Jiaxiang Tang, Hang Zhou, Xiaokang Chen, Tianshu Hu, Errui Ding, Jingdong Wang, and Gang Zeng. 2023b. Delicate Textured Mesh Recovery from NeRF via Adaptive Surface Refinement. In *International Conference on Computer Vision (ICCV)*.
- Peng Wang, Lingjie Liu, Yuan Liu, Christian Theobalt, Taku Komura, and Wenping Wang. 2021. Neus: Learning neural implicit surfaces by volume rendering for multi-view reconstruction. *arXiv preprint arXiv:2106.10689* (2021).
- Yiming Wang, Qin Han, Marc Habermann, Kostas Daniilidis, Christian Theobalt, and Lingjie Liu. 2023a. Neus2: Fast learning of neural implicit surfaces for multi-view

- reconstruction. In *Proceedings of the IEEE/CVF International Conference on Computer Vision*. 3295–3306.
- Yiqun Wang, Ivan Skorokhodov, and Peter Wonka. 2023b. PET-NeuS: Positional Encoding Triplanes for Neural Surfaces. (2023).
- Qiangeng Xu, Zexiang Xu, Julien Philip, Sai Bi, Zhixin Shu, Kalyan Sunkavalli, and Ulrich Neumann. 2022. Point-nerf: Point-based neural radiance fields. In *Proceedings of the IEEE/CVF Conference on Computer Vision and Pattern Recognition*. 5438–5448.
- Xiaofeng Yang, Yiwen Chen, Cheng Chen, Chi Zhang, Yi Xu, Xulei Yang, Fayao Liu, and Guosheng Lin. 2023a. Learn to Optimize Denoising Scores for 3D Generation: A Unified and Improved Diffusion Prior on NeRF and 3D Gaussian Splatting. *arXiv preprint arXiv:2312.04820* (2023).
- Ziyi Yang, Xinyu Gao, Wen Zhou, Shaohui Jiao, Yuqing Zhang, and Xiaogang Jin. 2023b. Deformable 3d gaussians for high-fidelity monocular dynamic scene reconstruction. *arXiv preprint arXiv:2309.13101* (2023).
- Zeyu Yang, Hongye Yang, Zijie Pan, Xiatao Zhu, and Li Zhang. 2024. Real-time Photorealistic Dynamic Scene Representation and Rendering with 4D Gaussian Splatting. In *International Conference on Learning Representations (ICLR)*.
- Lior Yariv, Jiatao Gu, Yoni Kasten, and Yaron Lipman. 2021. Volume rendering of neural implicit surfaces. *Advances in Neural Information Processing Systems* 34 (2021), 4805–4815.
- Lior Yariv, Peter Hedman, Christian Reiser, Dor Verbin, Pratul P. Srinivasan, Richard Szeliski, Jonathan T. Barron, and Ben Mildenhall. 2023. BakedSDF: Meshing Neural SDFs for Real-Time View Synthesis. *arXiv* (2023).
- Lior Yariv, Yoni Kasten, Dror Moran, Meirav Galun, Matan Atzmon, Basri Ronen, and Yaron Lipman. 2020. Multiview neural surface reconstruction by disentangling geometry and appearance. *Advances in Neural Information Processing Systems* 33 (2020), 2492–2502.
- Keyang Ye, Tianjia Shao, and Kun Zhou. 2023. Animatable 3d gaussians for high-fidelity synthesis of human motions. *arXiv preprint arXiv:2311.13404* (2023).
- Taoran Yi, Jiemin Fang, Guanjun Wu, Lingxi Xie, Xiaopeng Zhang, Wenyu Liu, Qi Tian, and Xinggang Wang. 2023. Gaussiandreamer: Fast generation from text to 3d gaussian splatting with point cloud priors. *arXiv preprint arXiv:2310.08529* (2023).
- Wang Yifan, Felice Serena, Shihao Wu, Cengiz Öztireli, and Olga Sorkine-Hornung. 2019. Differentiable surface splatting for point-based geometry processing. *ACM Transactions on Graphics (TOG)* 38, 6 (2019), 1–14.
- Alex Yu, Ruilong Li, Matthew Tancik, Hao Li, Ren Ng, and Angjoo Kanazawa. 2021. Plenotrees for real-time rendering of neural radiance fields. In *Proceedings of the IEEE/CVF International Conference on Computer Vision*. 5752–5761.
- Qiang Zhang, Baek Seung-Hwan, Rusinkiewicz Szymon, and Felix Heide. 2022. Differentiable point-based radiance fields for efficient view synthesis. In *ACM SIGGRAPH Asia 2022 Conference Proceedings*. 1–12.
- Wojciech Zielonka, Timur Bagautdinov, Shunsuke Saito, Michael Zollhöfer, Justus Thies, and Javier Romero. 2023. Drivable 3d gaussian avatars. *arXiv preprint arXiv:2311.08581* (2023).
- M. Zwicker, H. Pfister, J. van Baar, and M. Gross. 2001. Surface Splatting. In *ACM Transactions on Graphics (Proc. ACM SIGGRAPH)*. 371–378.